Available online at www.sciencedirect.com
SCIENCE DIRECT®
International Journal of Multiphase Flow 30 (2004) 585–614
International Journal of Multiphase Flow
www.elsevier.com/locate/ijmulflow

Advanced electromagnetic flowmetry for slug flow: numerical signal prediction and calibration

Deok Hong Kang [a,b], Yeh-Chan Ahn [a], Byung Do Oh [a], Moo Hwan Kim [a,*]

[a] *Department of Mechanical Engineering, Pohang University of Science and Technology, San 31, Hyoja-dong, Namgu, Pohang, Kyoungbuk 790-784, South Korea*

[b] *Energy Research Team, Research Institute of Science and Technology, San 32, Hyoja Dong, Pohang 790-330, South Korea*

Received 24 December 2003; received in revised form 5 May 2004

Abstract

The transient nature and complex flow geometries of two-phase gas–liquid flows cause fundamental difficulties when measuring flow velocity using an electromagnetic flowmeter. Recently, a current-sensing flowmeter was introduced to obtain measurements with high temporal resolution. In this study, current-sensing flowmeter theory was applied to measure the fast velocity transients in slug flows. To do this, the velocity fields of axisymmetric gas–liquid slug flow in a vertical pipe were obtained using volume-of-fluid (VOF) method and the virtual potential distributions for the electrodes of finite size were also computed using the finite volume method for the simulated slug flow. The output signal prediction for slug flow was carried out from the velocity and virtual potential (or weight function) fields. The flowmeter was numerically calibrated to obtain the cross-sectional liquid mean velocity at an electrode plane from the predicted output signal. Two calibration parameters are required for this procedure: a flow pattern coefficient and a localization parameter. The flow pattern coefficient was defined by the ratio of the liquid resistance between the electrodes for two-phase flow with respect to that for single-phase flow, and the localization parameter was introduced to avoid errors in the flowmeter readings caused by liquid acceleration or deceleration around the electrodes. These parameters were also calculated from the computed velocity and virtual potential fields. The results can be used to obtain the liquid mean velocity from the slug flow signal measured by a current-sensing flowmeter.
© 2004 Elsevier Ltd. All rights reserved.

Keywords: Current-sensing electromagnetic flowmeter; Virtual potential distributions; Slug flow; Weight function; Flow pattern coefficient; Localization parameter

* Corresponding author. Tel.: +82-54-279-2165; fax: +82-54-279-3199.
E-mail address: mhkim@postech.ac.kr (M.H. Kim).

0301-9322/$ - see front matter © 2004 Elsevier Ltd. All rights reserved.
doi:10.1016/j.ijmultiphaseflow.2004.04.010

1. Introduction

Electromagnetic flowmeters have been successfully applied to measure single-phase liquid mean velocities in various industries. There have also been continuous efforts made to measure the characteristics of two-phase flow using electromagnetic flowmeters, since such meters do not introduce a pressure drop and can provide a fast response to changes in the flow. Thus, there are many potential applications for electromagnetic flowmeters in two-phase flow.

The theory behind the voltage-sensing flowmeter was first developed by Shercliff (1954). The weight function, which represents the degree of the contribution of the fluid velocity to the signal in the cross-section of a conduit, was proposed and computed for single-phase flow. Bevir (1970) developed the weight vector $\mathbf{W} = \mathbf{B} \times \mathbf{j}$, which is an extension of the weight function to three-dimensions using the concept of a virtual current $\mathbf{j}$. Using the virtual current method, O'Sullivan and Wyatt (1983) derived rectilinear weight functions for various numbers, sizes, and shapes of electrodes for rectilinear flows. Wyatt (1986) analytically calculated a rectilinear weight function as a series solution for annular flow as well as single-phase flow. Zhang (1997) investigated the effect of the phase distribution on the rectilinear weight function in a two-dimensional annular domain with or without eccentricity, and proposed a new rectilinear weight function as a series solution. The estimated error of his series solution truncated up to a finite order increased as the film thickness of the annular flow decreased. Since the normalized film thickness of annular flow in practical situations is less than 0.1, a higher-order series solution was required to obtain an accurate solution. Zhang (1998) numerically studied the effect of a bubble on the virtual current of an electromagnetic flowmeter with the bubble located at various positions along the pipe axis. A two-dimensional assumption was used and the virtual potential was expressed in terms of a series. The effect of bubble size was also considered. The change of the virtual current caused by the existence of the bubble was represented using deviation and asymmetry. However, the calculation error increased to 24% as the bubble size normalized with the distance between electrodes increased to 0.9. Lim and Chung (1998) also used the weight function method, but in addition, they numerically solved the flowmeter equation using a finite volume method on the given velocity field. Their study was aimed at comparing the calculation accuracy of each method, which they determined strongly depended on the grid system.

There exist four regular flow patterns in two-phase flow in a vertical pipe; these can often be categorized phenomenologically into bubbly, slug, churn, and annular flows. To measure the liquid mean velocity (cross-sectional average) with an electromagnetic flowmeter, each flow pattern must be considered separately because of their different flow characteristics. Since bubbly flow can be approximated as a homogeneous mixture of gas and liquid at the same velocity, there are no additional measurement difficulties for this type of flow compared to single-phase flow. Cha et al. (2002) and Knoll (1991) reported that this approximation gives rise to no more than a 5% error in the liquid flow rate when the void fraction is less than 0.25. Annular flow measurements are also similar to those of single-phase flow if the film is assumed to be uniform and smooth, and the gas core is located at the center of the flow tube.

Of the regular two-phase flow patterns, slug flow is the most complicated, as the liquid axial velocity over a slug unit experiences considerable acceleration or deceleration. If one considers a cross-section of slug flow, it is composed of an annular flow when a Taylor bubble is passing by, and a bubbly flow when a liquid slug occupies the cross-section. Mi (1998) separated the time

series of the void fraction and liquid velocity into the two parts (annular and bubbly), and applied the appropriate theory to each. The decomposition greatly simplified the problem, but resulted in prediction error, as the velocity field of the slug flow violates the fully developed and rectilinear velocity field assumptions. In particular, the error became significant when the tail of a slug bubble passed by an electrode because of the strong deceleration in this region. This could be the main source of the 15% error reported by Mi (1998) in the liquid flow rate.

Slug flow measurements made with an electromagnetic flowmeter require a high temporal resolution because of the rapidly changing velocities. However, voltage-sensing flowmeters are vulnerable to noise due to power leakage (Tsiknakis, 1988). This error increases at the high-frequency excitation rate that is required for high temporal resolution measurements. Recently, a current-sensing flowmeter was introduced that inherently achieved a high temporal resolution (Ahn et al., 2003a). A simplified calibration process associated with the flow pattern coefficient, f, was also proposed. The output predictions, weight functions, and functional form of the flow pattern coefficients were obtained using three-dimensional virtual potential distribution computations in annular flow geometries (including single-phase flow).

To predict the output for a given velocity profile and to acquire the velocity information from the output, previous research has focused on the weight vector $\mathbf{W} = \mathbf{B} \times \mathbf{j}$ (3D), the rectilinear weight function (2D), and the axisymmetric weight function (1D). As will be discussed in detail in the next section, it is very useful to calculate the three-dimensional virtual potential distribution, G, instead of the weight vector (or function). The weight vector (or function) can easily be obtained by taking the gradient of the virtual potential. Also, the impedance between electrodes that is required to obtain the flow-induced emf from the output of the current-sensing flowmeter is equal to the difference between the virtual potentials, ΔG, at two electrodes if the contact impedances between the liquid and the electrodes can be neglected. Furthermore, knowledge of the virtual potential distribution enables us to investigate the effect of an arbitrary velocity field on the flowmeter output, which means that the previous theory of electromagnetic flowmeters is not restricted to rectilinear, axisymmetric, and fully developed flow fields. For example, an electromagnetic flowmeter can measure a liquid's velocity subject to considerable acceleration and deceleration in a two-phase slug flow. In addition, the three-dimensional virtual potential distribution is important to obtain the localization parameter, χ, and the flow pattern coefficient, f, which will be introduced in the next section. The localization parameter gives the local mean velocity of a developing flow from an electromagnetic flowmeter reading. The flow pattern coefficient has been proposed to simplify the calibration process for two-phase flows, and is defined by the ratio of the liquid resistance between electrodes for the two-phase flow with respect to that for a single-phase flow (Ahn et al., 2003a).

Signal prediction and calibration are major concerns when using current-sensing electromagnetic flowmeters for slug flow measurements. In this study, therefore, the three-dimensional virtual potential and velocity distributions were numerically computed for slug flows, and then used to obtain the localization parameters and flow pattern coefficients, as well as the weight functions.

2. Electromagnetic flowmeter theory

In voltage-sensing flowmeters (see Fig. 1(a)), there are unpredictable stray currents (i_1 and i_2) that are caused by power leakage flows through the double layers between the electrodes and the

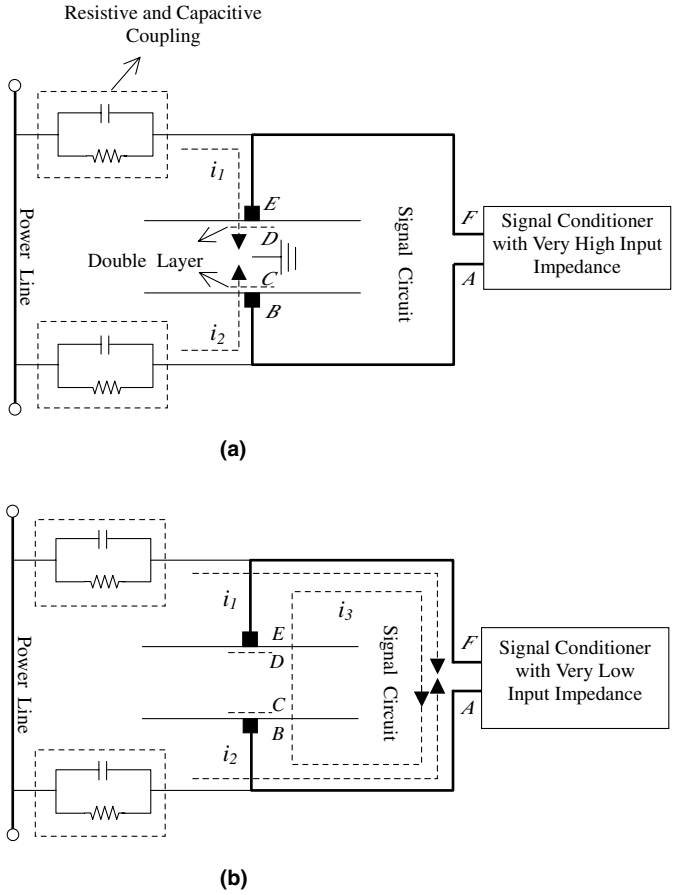

Fig. 1. A voltage-sensing flowmeter versus a current-sensing flowmeter (Ahn et al., 2003a). (a) Voltage-sensing flowmeter, (b) current-sensing flowmeter.

liquid to the ground in the liquid because of the signal conditioner, which has a very high input impedance. These currents produce unpredictable voltages at terminals A and F due to the contact impedance of the layer and the resistance of the liquid. Since the impedances along the two stray current paths, i_1 and i_2, are not symmetric to each other, the two voltages at terminals A and F cannot be nullified by common-mode rejection; the remaining portion of the voltage becomes the power leakage noise. (Note that the resistances of the liquid between points C or D and the ground vary with respect to the two-phase flow configurations in the conduit.) The noise voltage is much larger than the flow-induced emf. The stray current problem becomes more serious as the excitation frequency increases, since the capacitive coupling between the signal and power circuits becomes stronger and a higher voltage is required across the coil if the same magnet current (or magnet field strength) is to be provided. However, high frequency excitation is required to obtain a high temporal resolution.

On the other hand, current-sensing flowmeters (see Fig. 1(b)) use a signal conditioner with very low input impedance (Yu et al., 1997) to measure the current from flow-induced emf. The

unpredictable stray currents (i_1 and i_2), caused by the power leakage, flow to the signal conditioner, not the fluid. They become noise currents mixed with the signal current, i_3, from the flow-induced emf. The stray currents are not dependent on the contact impedance or the liquid resistance, but rather on the capacitive and resistive coupling between the signal and power circuits. This leaves more room for canceling the two opposite currents i_1 and i_2 than with the voltage-sensing flowmeter. If appropriate shielding is provided around the electromagnet windings and signal wires, the noise currents can mostly be cancelled out, despite the high-frequency excitation. Another important point about current-sensing flowmeters is the relevance of the signal current i_3 to the contact impedance and liquid resistance in a conduit. To predict the signal current i_3 from the flow-induced emf, the impedances along the paths of the signal current i_3 must be evaluated. The liquid resistance is related to the liquid conductivity (sensitive to temperature) and configuration of the two-phase flow. As the liquid conductivity and flow configuration in a two-phase flow vary with time, the signal current i_3 changes. The signal current i_3 is affected by the contact impedances of the double layers (or by the impedance between the liquid and the electrodes). The contact impedance is very sensitive to the electrode material and the electrochemical properties of the liquid. In the field of electrochemistry, there has been extensive discussion of this problem (Glasstone, 1942; Macdonald, 1987).

In short, current-sensing flowmeters are immune to the noise caused by power leakages, and guarantee the ability to measure the signal current, i_3, caused by the flow-induced emf. However, to predict the liquid velocity from the signal current is complicated, because the impedances along the paths of i_3 must be evaluated.

For conventional voltage-sensing flowmeters, the potential distribution U inside a flow tube is described by the Poisson equation (Shercliff, 1962; Bevir, 1970). The potential difference ΔU between two electrodes can be represented by

$$\Delta U \cdot (1\mathrm{A}) = \int \int_{\tau} \int \mathbf{v} \cdot \mathbf{W} \, \mathrm{d}\tau, \tag{1}$$

where $\mathbf{v}$ is the velocity vector, τ is the volume, and $\mathbf{W} = \mathbf{B} \times \mathbf{j}$ is the weight vector, which is the cross-product of the magnetic flux density $\mathbf{B}$ and the virtual current density $\mathbf{j}$. Note that the dimensions on both sides of Eq. (1) are volts times amperes [VA], not volts [V], since the unit virtual current, which is represented by (1A) on the left-hand side of the equation, can be omitted usually. Evaluating the potential difference from Eq. (1) needs a virtual problem: obtaining the distribution of the virtual current density $\mathbf{j}$ in the stationary flow with a unit current flowing through the electrodes at the boundary. Thus, $\mathbf{j}$ depends on the shape of the electrode, electrical conditions on the flowmeter wall, and flow configurations (for a two-phase flow). When the induced magnetic field is small and the conductivity is uniform (if not stated explicitly, this shall be assumed), $\nabla \times \mathbf{B} = 0$ and $\nabla \times \mathbf{j} = 0$. There exist corresponding harmonic potentials, H and G, associated with B and j, respectively; these are $\mathbf{B} = \nabla H$, $\mathbf{j} = \nabla G$.

For several restricted flow fields in an annulus, the volume integral in Eq. (1) reduces to

$$\int \int_{\tau} \int \mathbf{v} \cdot \mathbf{W} \, \mathrm{d}\tau = \int_0^{2\pi} \int_{R_\mathrm{i}}^{R} W(r,\theta) v_z(r,\theta) r \, \mathrm{d}r \, \mathrm{d}\theta, \tag{2}$$

for rectilinear and fully developed flow fields, and

$$\int\int_{\tau}\int \mathbf{v}\cdot\mathbf{W}\,\mathrm{d}\tau = 2\pi\int_{R_\mathrm{i}}^{R} W'(r)v_z(r)r\,\mathrm{d}r, \tag{3}$$

for rectilinear, axisymmetric, and fully developed flow fields. Here, $W(r,\theta)$ is the rectilinear weight function, $W'(r)$ is the axisymmetric weight function, R is the pipe inner radius, and R_i is the radius of the gas core ($R_\mathrm{i}=0$ for single-phase flow). The weight functions are given by

$$W(r,\theta) = \int_{-\infty}^{\infty} W_z\,\mathrm{d}z \tag{4}$$

and

$$W'(r) = \frac{1}{2\pi}\int_0^{2\pi} W(r,\theta)\,\mathrm{d}\theta, \tag{5}$$

where $W_z = Bj_y$ for a uniform transverse magnetic field B. It can easily be shown using the mean value theorem for the harmonic function (Wyatt, 1986) that, for a uniform transverse magnetic field and point-electrode,

$$W'(r) = \mathrm{const} = \frac{2B\cdot(1\mathrm{A})}{\pi R(1-\varepsilon)}, \tag{6}$$

where ε is the void fraction ($\varepsilon=0$ for single-phase flow). Therefore,

$$\int\int_{\tau}\int \mathbf{v}\cdot\mathbf{W}\,\mathrm{d}\tau = \frac{2B\cdot(1\mathrm{A})}{\pi R(1-\varepsilon)}Q_\mathrm{L} = 2Bv_\mathrm{m}R\cdot(1\mathrm{A}). \tag{7}$$

Here, Q_L is the liquid volumetric flowrate and v_m is the liquid (cross-sectional) mean velocity. Even though Eq. (7) was derived for two-phase annular or single-phase liquid flows, it also holds for two-phase bubbly flows, which can be considered homogeneous gas–liquid mixtures with the same velocity.

Electromagnetic flowmeter theory has been applied mainly to rectilinear, axisymmetric, and fully developed flow fields. This does not describe two-phase flows in general. For example, the liquid velocity field along a slug unit experiences considerable acceleration and deceleration in slug flow (Mi et al., 2001).

For a rapidly accelerated and decelerated flow with an axisymmetric velocity field and geometry, such as a slug flow, the volume integral in Eq. (1) reduces to

$$\int\int_{\tau}\int \mathbf{v}\cdot\mathbf{W}\,\mathrm{d}\tau = 2\pi\int\int [v_r(r,z)W_r(r,z)+v_z(r,z)W_z(r,z)]r\,\mathrm{d}r\mathrm{d}z \equiv \frac{2Bv_\mathrm{m}R\cdot(1\mathrm{A})}{\chi}. \tag{8}$$

Here, χ is a localization parameter, $v_r(r,z)$ and $v_z(r,z)$ are the r- and z-components of the velocity vector $\mathbf{v}$, respectively, $W_r(r,z)$ is the radial weight function, and $W_z(r,z)$ is the axial weight function. The weight functions are defined by

$$W_r(r,z) = \frac{1}{2\pi}\int_0^{2\pi} W_r(r,\theta,z)\,\mathrm{d}\theta = -\frac{B}{2\pi}\int_0^{2\pi}\sin\theta\frac{\partial G}{\partial z}\,\mathrm{d}\theta \tag{9}$$

and

$$W_z(r,z) = \frac{1}{2\pi}\int_0^{2\pi} W_z(r,\theta,z)\,\mathrm{d}\theta = \frac{B}{2\pi}\int_0^{2\pi}\frac{\partial G}{\partial y}\,\mathrm{d}\theta \tag{10}$$

for a uniform transverse magnetic field **B**. Here, G denotes the virtual potential; its gradient is the virtual current $\mathbf{j} = \nabla G$. An electromagnetic flowmeter gives the volume-averaged value of the velocity, not the local value at the electrodes. Therefore, a localization parameter χ is required to obtain the local liquid mean velocity from the flowmeter output. This parameter is related to the flow configuration and the velocity profile. In general, the radial velocity, $v_r(r,z)$ in Eq. (8) is negligible in a liquid film compared to the axial velocity, $v_z(r,z)$. In addition, the radial weight function tends to be localized near the pipe wall in the wake zone (this will be shown in Section 3.2.2) and the radial velocity is negligible near the wall. Therefore, the axial velocity contribution dominates the target signal (see Fig. 15 and Section 3.2.2).

The same virtual problem that was introduced for voltage-sensing flowmeters is also useful for current-sensing flowmeters. The current output, i can be described without the contact impedances in the double layers by

$$i = \frac{\int\int_\tau \int \mathbf{v}\cdot\mathbf{W}\,\mathrm{d}\tau}{\Delta G}, \tag{11}$$

where ΔG is the virtual potential difference between finite-sized electrodes with small cross-sectional areas, and is equivalent to the fluid resistance between the electrodes. In comparison with voltage-sensing meters, both have the same volume integral, $\int\int_\tau \int \mathbf{v}\cdot\mathbf{W}\,\mathrm{d}\tau$, and **W** is related to the gradient of the virtual potential G. The calculation of the virtual potential G is very useful for both types of flowmeter, as G is related to the effect of arbitrary velocity fields on the flowmeter output. When the transverse magnetic field is uniform and finite-sized electrodes are used, Eq. (11) gives

$$i_{\mathrm{SP}} = \frac{2Bv_{\mathrm{mSP}}R\cdot(1\mathrm{A})}{\Delta G_{\mathrm{SP}}} \tag{12}$$

for single-phase liquid flow, and

$$i_{\mathrm{TP}} = \frac{2Bv_{\mathrm{mTP}}R\cdot(1\mathrm{A})}{\chi\Delta G_{\mathrm{TP}}} \tag{13}$$

for two-phase flow ($\chi = 1$ for bubbly and annular flow, $\chi \neq 1$ for slug flow). Here, v_{m} is liquid mean velocity, and the subscripts SP and TP denote single- and two-phase flows, respectively. Hence, i_{TP} can be rewritten using Eqs. (12) and (13), see Ahn et al. (2003a), as

$$i_{\mathrm{TP}} = \frac{i_{\mathrm{SP}}}{v_{\mathrm{mSP}}}\frac{1}{f}\frac{v_{\mathrm{mTP}}}{\chi}, \tag{14}$$

where f is the flow pattern coefficient, which was defined previously, and is related only to the flow configuration. Therefore, the calculation of the three-dimensional virtual potential distribution G also gives the flow pattern coefficient f for current-sensing flowmeters. The output of current-sensing flowmeters is dependent on the liquid resistance, ΔG_{TP}, between the electrodes, neglecting the contact impedance in the double layer. The liquid resistance is related to the liquid conductivity (sensitive to temperature) and the flow configuration. By introducing the flow pattern coefficient f and using a calibration chart for single-phase flow (that includes the effects of

temperature and fluid species), one can separate the dependency of the output on the flow configuration from the liquid conductivity.

In practical applications to slug flows, a single-phase flow calibration chart, the functional forms of the flow pattern coefficient f, and the localization parameters χ are required. The single-phase flow calibration chart from the manufacturer gives the $\frac{j_{SP}}{v_{mSP}}$ term in Eq. (14). The slug flow configurations can easily be measured using at most two impedance meters (the void fraction of the film thickness, void propagation speed, and bubble length can be obtained). If the functional form of f with respect to the flow configuration is obtained numerically or experimentally in advance (for example, by using impedance spectroscopy), the measured flow configurations give the value of f. The localization parameter χ can also be evaluated by computing the flow field and the virtual potential distribution for a given flow geometry. Therefore, the current output i_{TP} can be used to obtain an actual liquid mean velocity for slug flow.

The liquid mean velocity from the flowmeter output can be rewritten for both voltage- and current-sensing flowmeters as (see Eq. (8))

$$v_{m,TP}|_{z=\text{Electrode}} = \chi \int [\bar{v}_r(z)q(z) + \bar{v}_z(z)p(z)]\,dz, \tag{15}$$

where

$$p(z) \equiv \int \frac{\pi W_z(r,z)}{BR\cdot(1\text{A})} r\,dr, \tag{16}$$

$$q(z) \equiv \int \frac{\pi W_r(r,z)}{BR\cdot(1\text{A})} r\,dr, \tag{17}$$

$$\bar{v}_z(z) \equiv \frac{1}{p(z)} \int v_z(r,z) \frac{\pi W_z(r,z)}{BR\cdot(1\text{A})} r\,dr, \tag{18}$$

$$\bar{v}_r(z) \equiv \frac{1}{q(z)} \int v_r(r,z) \frac{\pi W_r(r,z)}{BR\cdot(1\text{A})} r\,dr. \tag{19}$$

Here, $v_{mTP}|_{z=\text{Electrode}}$ denotes the liquid mean velocity on the electrode plane, $p(z)$ is an axial weight density function because its integral with respect to z is unity from the mean-value theorem of the harmonic function, $q(z)$ is a radially integrated radial weight function, $\bar{v}_z(z)$ is the radially weighted axial velocity, and $\bar{v}_r(z)$ is the radially weighted radial velocity.

3. Numerical analysis

To obtain the flow pattern coefficient f and the localization parameter χ, we performed numerical simulations of the two-dimensional axisymmetric slug flow in a vertical pipe, and computed the three-dimensional virtual potential distributions for a rising slug flow.

3.1. Numerical simulation of slug flow

3.1.1. Numerical method

The simulation of a Taylor bubble rising in a 25.4-mm diameter vertical pipe was performed using the volume-of-fluid (VOF) model that is implemented in the CFD-ACE+ code (CFD Research Corporation, Version 2002.2.24). The bubble passed through a stagnant liquid with a density equal to 1000 kg/m^3 and was subject to gravitational acceleration of 9.8 m/s^2. The computational domain and initial bubble shape are shown in Fig. 2. The effective domain in the axial direction, which influences the electromagnetic flowmeter output, was previously reported to be a distance within ±2 times of a pipe radius of R from the electrode location (Ahn et al., 2003a). Hereafter, the region around the electrode will be called the *effective flowmeter window* because it covers most of the weighting area (see Section 3.2.2). In this study, therefore, two slug bubble lengths were considered: one that was longer than $4R$ and one that was shorter than $4R$. The longer bubble was initially $5.6R$, and the shorter bubble was initially $2.0R$. These grew to $6.1R$ and $2.9R$, respectively. The computational domain was $40R$, which was sufficient to obtain the quasi-steady Taylor bubble shape and the rising velocity. An axisymmetric cylindrical coordinate system, (r, z), was used in the analysis.

The transient two-dimensional Navier–Stokes equations and the continuity equation for an incompressible fluid are given by

$$\frac{\partial v_r}{\partial t} + v_r \frac{\partial v_r}{\partial r} + v_z \frac{\partial v_r}{\partial z} = -\frac{1}{\rho}\frac{\partial p}{\partial r} + \frac{\mu}{\rho}\left(\frac{\partial^2 v_r}{\partial r^2} + \frac{1}{r}\frac{\partial v_r}{\partial r} + \frac{\partial^2 v_r}{\partial z^2} - \frac{v_r}{r^2}\right), \tag{20}$$

$$\frac{\partial v_z}{\partial t} + v_r \frac{\partial v_z}{\partial r} + v_z \frac{\partial v_z}{\partial z} = -\frac{1}{\rho}\frac{\partial p}{\partial z} + \frac{\mu}{\rho}\left(\frac{\partial^2 v_z}{\partial r^2} + \frac{1}{r}\frac{\partial v_z}{\partial r} + \frac{\partial^2 v_z}{\partial z^2}\right) + g, \tag{21}$$

$$\frac{\partial v_r}{\partial r} + \frac{\partial v_z}{\partial z} + \frac{v_r}{r} = 0. \tag{22}$$

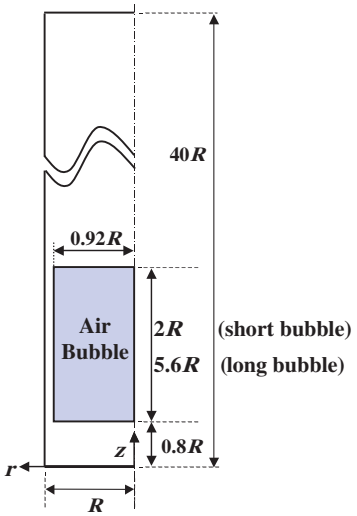

Fig. 2. Computational domain and initial bubble shape.

In these equations, v_r and v_z are the radial and axial components of the velocity, respectively, t is time, ρ is the density, g is the acceleration due to gravity, r and z are the radial and axial coordinates, and p is the pressure. These equations were solved with appropriate boundary conditions: an axisymmetric condition at $r = 0$, and a no-slip condition along all solid boundaries. The governing equations were discretized using a finite volume method (Patankar, 1980) on a non-uniform cylindrical mesh. A first-order upwind scheme was applied to interpolate the cell-face values in the convective terms. The liquid was initially quiescent and the flow was simulated in a frame of stationary coordinate systems.

The position of the moving gas–liquid interface in the solution domain was defined by the fraction volume of liquid fluid F (Hirt and Nichols, 1981), which was determined by solving a transport equation,

$$\frac{\partial F}{\partial t} + \frac{v_r}{r}\frac{\partial (rF)}{\partial r} + v_z \frac{\partial F}{\partial z} = 0. \tag{23}$$

To capture the sophisticated dynamics of the interface, piecewise linear interface reconstruction (PLIC, Kothe et al., 1996) was used. In this work, the net normal force due to the surface tension was given by Yang et al. (1998),

$$\mathbf{F}_S = \int \sigma \mathbf{n} \times \mathrm{d}\mathbf{x}, \tag{24}$$

where σ is the surface tension between the two fluids (in this study, assumed constant at 0.0725 N/m), $\mathbf{x}$ gives the edges of the interfaces within the individual computational cells, and $\mathbf{n}$ is the unit normal of the interface, given by

$$\mathbf{n} = \nabla F. \tag{25}$$

The net normal force in Eq. (24) was used as a body force in the momentum equations, Eqs. (20) and (21). Since an explicit technique was used to discretize the transport equation, Eq. (23), the CFL (Courant–Friedrichs and Lewy) condition must be satisfied when selecting a time step. In this work, the time step varied over the run matrix, but 10^{-5} s was a typical value.

The semi-implicit method for pressure-linked equations (SIMPLEC, van Doormaal et al., 1984) was adopted for the velocity–pressure coupling, and the resultant non-symmetrical system arising from the momentum equation was solved using the conjugate gradient squared (CGS) method with incomplete Cholesky preconditioning (Saad, 1996). The resulting symmetric system due to the pressure correction was solved using algebraic multigrid (AMG) techniques (Lonsdale, 1993). The convergence criterion for each time step stated that the residuals for each variable must be reduced at least by a given criterion (10^{-4} in the present computations).

The grid dependence was investigated using three grid sizes: 67×988, 45×656, and 57×1750 in the radial and axial directions, respectively. The maximum change in the bubble rising speed obtained using these grids was less than 1.5%. However, the grid size affected the extent of the non-physical small trailing bubbles that were computed in the wake of the Taylor bubble. DeJesus (1997) reported that PLIC VOF methods tend to introduce small non-physical void or fluid remnants when the flow has substantial vorticity, such as in the wake zone of a Taylor bubble. Therefore, the results reported in this study were obtained using the largest grid with 57×1750 grid points, which revealed the smallest number of satellite bubbles. The normalized mesh size in

the z-direction, $\Delta z^* = \Delta z/R$, was uniform at 0.0225. The normalized mesh size in the r-direction was non-uniform, expanding in size, with $\Delta r^* = \Delta r/R$ ranging from 0.0131 near the pipe wall to 0.0188 near the pipe axisymmetric axis.

3.1.2. Numerical results and comparison with experiments

Although many researchers have investigated the structure of gas–liquid slug flow in a vertical pipe, few film velocity measurements have been reported in the literature. This is because these measurements are difficult to perform because the liquid film is very thin (on the order of one millimeter) and can be easily disturbed, thus altering the flow field. To the authors' knowledge, only two sets of experimental results of liquid film velocity measurements are available. DeJesus et al. (1995) presented the first measurements of velocity profiles in the liquid phase surrounding a single Taylor bubble rising through a stagnant liquid in a vertical pipe, using photochromic dye activation and image analysis. Polonsky et al. (1999) measured the liquid film velocity field around a Taylor bubble rising through stagnant and moving liquid in a vertical pipe using a PIV (particle image velocimetry) technique, and reported the averaged liquid film velocity. There are some slight deviations between the two sets of data.

Kawaji et al. (1996) used the VOF method to predict the shape of a bubble rising in stagnant liquid in a vertical pipe 25.6 mm in diameter. They compared these predictions with their own measurements. The predicted and measured bubble shapes were in good agreement with the potential flow solution obtained by Dumitrescu (1943). Bugg et al. (1998) used the VOF method to predict the Taylor bubble shape and terminal rise velocity. Their predictions spanned a wide range of *Eötvös* (Eo) and Morton numbers (Mo): $10 < Eo = \frac{\rho_L g D^2}{\sigma} < 100$ and $10^{-12} < Mo = \frac{g\eta_L^4}{\rho_L \sigma^3} < 10$. In these groups D is the pipe diameter, and η_L is the dynamic viscosity of the liquid. Anglart (2001) solved the transient, three-dimensional Navier–Stokes equations, both inside and outside a moving Taylor bubble, using the CFX4.2 code, and predicted the bubble shape, bubble speed, and pressure and velocity distributions, as well as the wall shear stress. Using these results, proper closure relationships for the interfacial forces and a new model for bubble-induced turbulence in slug flows have been proposed for two-fluid slug flow models.

Fig. 3 shows an example of the calculated long bubble shape evolution for $Eo = 87$, $Mo = 1.4 \times 10^{-11}$, and Froude number $Fr = 0.317$. The simulated bubble shape was obtained by contouring the $F = 0.5$ values. The evolution of the interfacial shape up to $t = 2.43$ s did not progress in a smooth fashion. Due to the interaction with vortices, a force was imparted on the base of the Taylor bubble which, by $t = 0.401$ s, resulted in a physically unrealistically large gas skirt and liquid cavity (DeJesus, 1997). However, thereafter the computation revealed a stable interface shape, except for the lower part of the Taylor bubble, which had not yet developed significantly. White and Beardmore (1962) stated that an inertia-controlled regime is realized, in which the bubbles have flat or concave bottoms, if the dimensionless inverse viscosity, $N_f = (Eo^3/Mo)^{1/4} > 550$. Bugg et al. (1998) proposed a clearer criterion, $Fr(= U_{TB}/\sqrt{gD}) > 0.3$. In this group U_{TB} is the Taylor bubble rise velocity. In the current study, both criteria were satisfied ($N_f = 14,766$ and $Fr = 0.317$); therefore, the present results showed the same trend for the bubble trailing edge as described by Bugg et al. (1998). In the present study, the Taylor bubble shape and velocity field at $t = 2.43$ s were deemed to be quasi-steady results, and were used to assess and calibrate the flowmeter output for slug flow. Hereafter, any reference to the Taylor bubble implies the conditions that existed at $t = 2.43$ s.

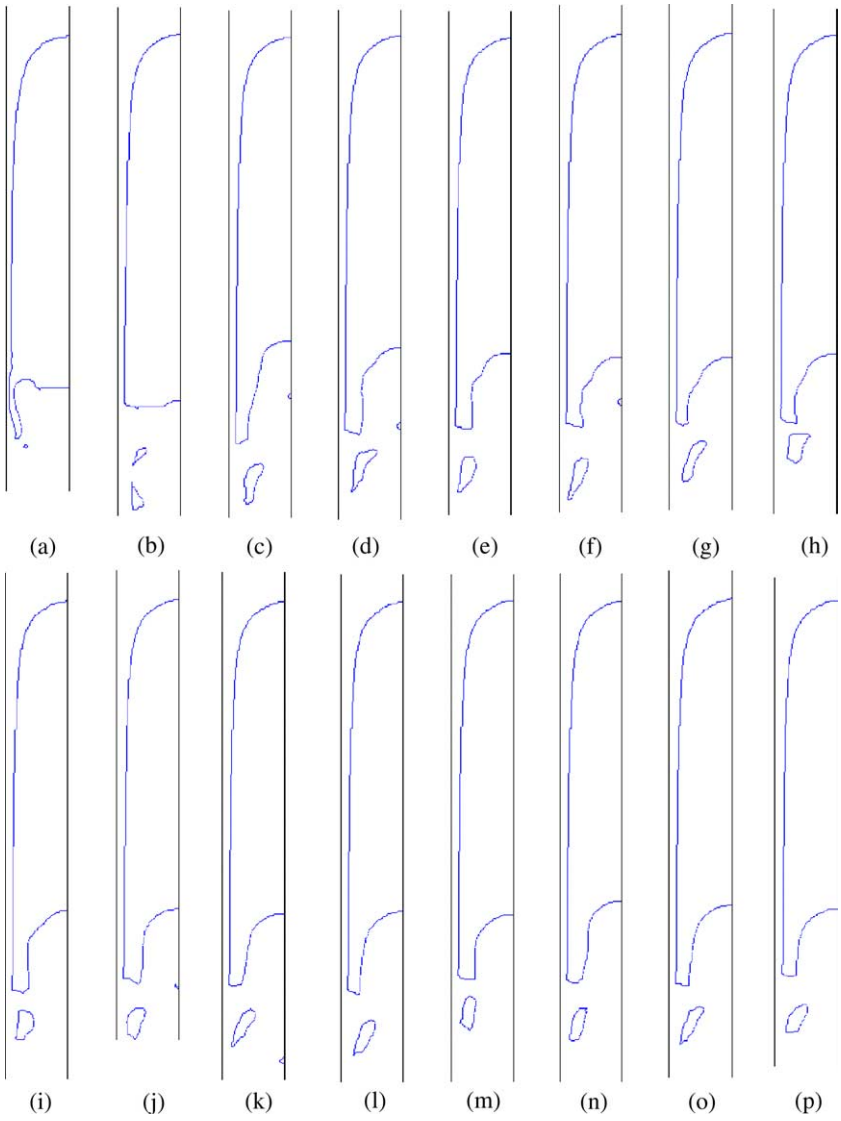

Fig. 3. Evolution of a long Taylor bubble shape for $Eo = 87$, $Mo = 1.4 \times 10^{-11}$ and $Fr = 0.317$: (a) $t = 0.11$ s; (b) $t = 0.25$ s; (c) $t = 0.401$ s; (d) $t = 0.54$ s; (e) $t = 0.69$ s; (f) $t = 0.84$ s; (g) $t = 1.01$ s; (h) $t = 1.184$ s; (i) $t = 1.34$ s; (j) $t = 1.51$ s; (k) $t = 1.65$ s; (l) $t = 1.81$ s; (m) $t = 1.99$ s; (n) $t = 2.16$ s; (o) $t = 2.30$ s; (p) $t = 2.43$ s.

Fig. 4 shows the variation of the film thickness, δ, with the distance from the top of the bubble, L_n, in the present numerical simulations with $Eo = 87$ and $Mo = 1.4 \times 10^{-11}$. There is one set of numerical results and three additional sets of experimental data also shown. These data were taken from Anglart (2001) for $Eo = 30$ and $Mo = 1.4 \times 10^{-11}$, DeJesus et al. (1995) for $Eo = 194$ and $Mo = 2.9 \times 10^{-9}$, Kawaji et al. (1996) for $Eo = 232$ and $Mo = 3.06 \times 10^{-9}$, and Mao and Dukler (1991) for $Eo = 337$ and $Mo = 2.5 \times 10^{-12}$. The present numerical results fall well within the existing experimental and numerical data.

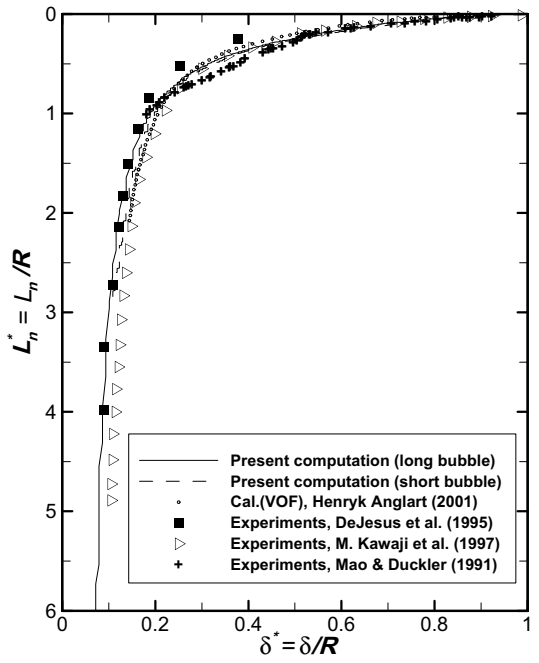

Fig. 4. Comparison of the computed film thickness δ^* with experimental data.

The theoretical rise velocity of a Taylor bubble in quiescent liquid inside a closed pipe of diameter D is given by

$$U_{\mathrm{TB}} = Fr\sqrt{gD}, \tag{26}$$

where $Fr = 0.34$–0.36. The present numerical results gave a Taylor bubble rise velocity of 0.158 m/s ($Fr = 0.317$). Therefore, the rise velocity was underpredicted, but it was within 10% of the theoretical value given by Eq. (26).

Detailed representations of the predicted velocity fields for long and short bubbles are shown in Fig. 5(a) and (b). These figures show the velocity vectors and lines of constant stream function for liquid and gas phases, including axial liquid velocity component profiles at various axial locations. The velocity fields indicated the expected characteristics. Since these were both inertia-dominated flows ($Fr > 0.05$, $Eo > 70$ and $N_{\mathrm{f}} > 550$, guidelines developed by White and Beardmore, 1962), the axial velocity profile in the film was nearly flat. However, it did increase with the axial position, resulting in a continuously thinning film all the way to the trailing edge. A recirculation zone was apparent in the wake region of the Taylor bubble for both cases. This zone was driven by the relatively high velocity wall jet penetrating the region below the bubble.

Fig. 6 shows the computed radially averaged film velocity for $Eo = 87$ and $Mo = 1.4 \times 10^{-11}$. The result was compared to the experimental work of DeJesus et al. (1995), which provided detailed velocity measurements around a rising Taylor bubble for $Eo = 100$ and $Mo = 1.0 \times 10^{-12}$. Both cases were in the regime where the surface tension forces ($Eo > 70$) and viscosity ($N_{\mathrm{f}} > 550$) were negligible (see White and Beardmore, 1962).

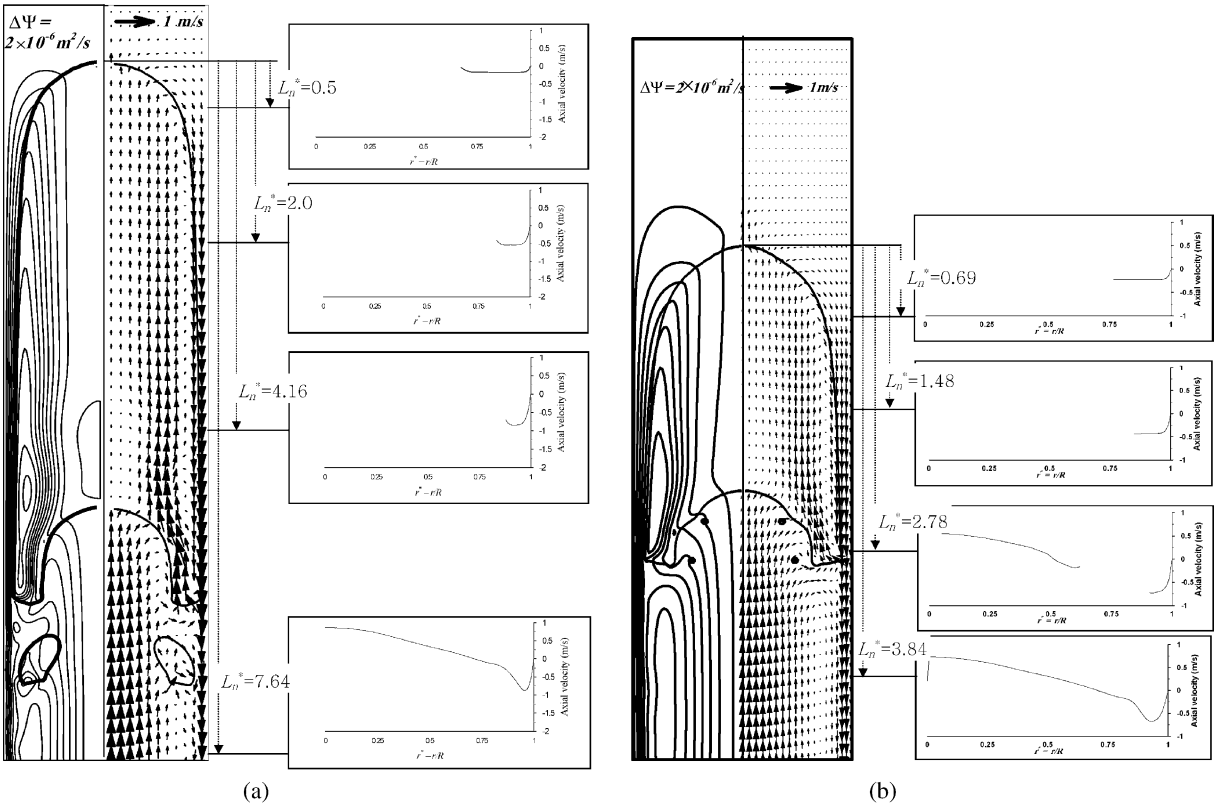

Fig. 5. Detailed velocity field information for $Eo = 87$, $Mo = 1.4 \times 10^{-11}$ and $Fr = 0.317$. The plots at the right give the axial velocity components. The left half of the contour plot shows lines of constant stream function while the right half shows velocity vectors: (a) long bubble, (b) short bubble.

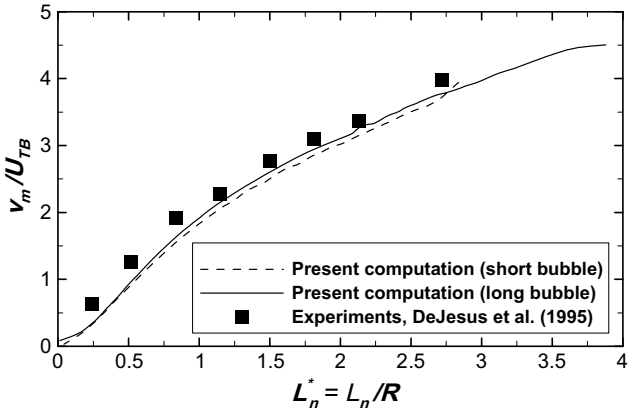

Fig. 6. Computed average film velocity v_m for $Eo = 87$, $Mo = 1.4 \times 10^{-11}$ and $Fr = 0.317$, compared to experimental data.

The numerically predicted Taylor bubble shapes and liquid-phase velocity distributions for both the long and short bubbles agreed well with the available data. These data were used to perform the signal prediction and calibration tasks for the current-sensing electromagnetic flowmeter in the next section.

3.2. Numerical computation of the virtual potential

3.2.1. Numerical method

The Taylor bubble shapes obtained numerically in the previous section were used to assess the flowmeter output when measuring slug flow. In this study, the two-dimensional axisymmetric Taylor bubble shapes were rotated about the axisymmetric axis (see Fig. 2) to generate three-dimensional bubbles. Although the small bubbles that are typically trapped between two Taylor bubbles in a slug flow are roughly spherical, the unrealistic small bubbles in the wake of the Taylor bubble (see Fig. 5(a)) were toroid in light of the assumed axial symmetry in the two-dimensional slug flow. In this work, therefore, the small bubbles were regarded as toroids revolved about the axis of symmetry. To solve the introduced virtual problem, the governing equation for the virtual potential G can be written in cylindrical coordinates as

$$\nabla^2 G = \frac{1}{r}\frac{\partial}{\partial r} r \frac{\partial}{\partial r} G + \frac{1}{r^2}\frac{\partial^2}{\partial \theta^2} G + \frac{\partial^2}{\partial z^2} G = 0 \tag{27}$$

for the computational domain shown in Fig. 7, where L is the axial length of the computational domain, L_b is the length of the slug bubble, L_e is the length of the square electrode for the computation, L_n is the nose location of the slug bubble, L_t is the tail location of the slug bubble and L_z is the half of the effective window.

The homogeneous Neumann condition was used at the boundary in the axial (z)-direction, since an infinite domain was assumed and current cannot pass through the end planes. When the size of flowmeter window around the electrode $L_z^* = L_z/R$ is greater than 4, it is sufficient to perform the computations without considering the end effects for annular flow provided $\delta^* = \delta/R = 0.05$ to 1.0 (see Ahn et al., 2003a). In this computation, the axial extent $L^*(L/R = 14.96)$ was determined to provide a sufficiently large domain that would not disturb the results, considering the positions of the various electrodes. In the azimuthal (θ) direction, the skew symmetric condition (see Fig. 7) was applied at the boundaries, as the two electrodes were located at mutually symmetric locations. Therefore, the computational domain was composed of only half of the cylinder, and the homogeneous Dirichlet condition was imposed at the center plane (with respect to the electrodes). In the radial (r) direction, a step-like distribution was used at the electrodes and a homogeneous Neumann condition was used at remaining locations along the pipe wall. The electrode was square and $L_e/R = 1/6.35$ in size. The boundary conditions can be summarized as follows:

$$\frac{\partial G}{\partial z} = 0 \text{ at } z = \text{upper and lower end planes}, \tag{28}$$

$$G = 0 \text{ at } \theta = 0 \text{ and } \theta = \pi, \tag{29}$$

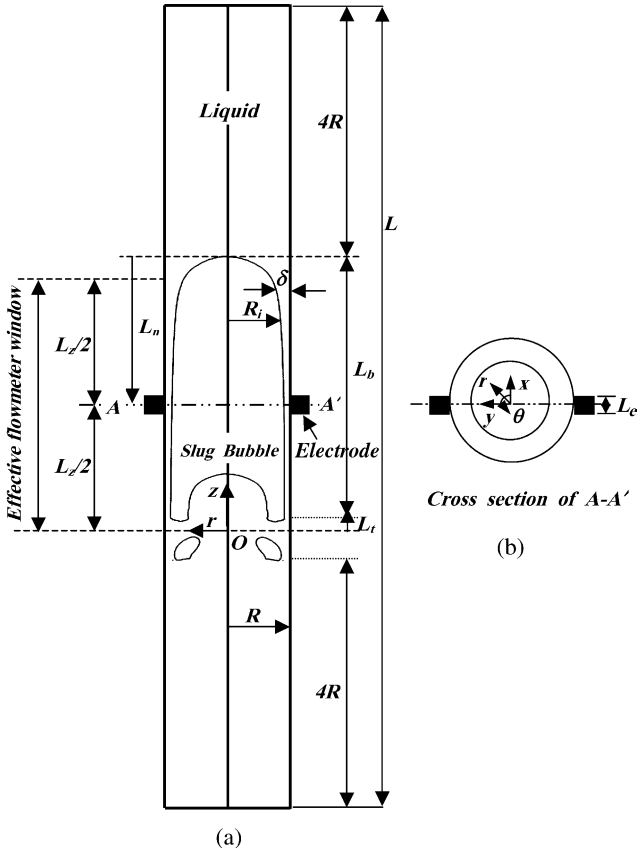

Fig. 7. Schematic diagram of the computational domain for the three-dimensional virtual potential.

$$\frac{\partial G}{\partial r} = E(\theta, z) \text{ at } r = R, \text{ on the electrode,} \tag{30}$$

$$\frac{\partial G}{\partial r} = 0 \text{ at } r = R, \text{ otherwise,} \tag{31}$$

$$\frac{\partial G}{\partial r} = 0 \text{ at } r = \text{interface.} \tag{32}$$

To solve the described three-dimensional virtual problem, numerical computations were performed using the CFD-ACE+ code (CFD Research Corporation, version 2002.2.24) because of the complex geometries involved. A finite volume method was used to solve the governing equation. A blending scheme (10% of the first-order upwind scheme plus 90% of a higher-order scheme) was used for the spatial discretization to provide for a stable and accurate numerical analysis. When the residual of G was less than the given criterion (10^{-10} in the present computation), G was considered to be converged.

The grid was located outside the bubble region, and a tetrahedral mesh was used in these simulations. The grid dependence was tested by doubling the total number of grid points for each

case (0.5×10^6 points and 1.0×10^6 points). The difference between the maximum potential value obtained using each grid was less than 0.2%. Therefore the simulations were performed with 0.5×10^6 points.

The solutions depended only on the electrode shape, once the overall geometry and the magnitude of the current on the electrodes were determined. In previous two-dimensional simulations (Zhang, 1997), the electrode was assumed to be a point so that the delta function could be used for the boundary condition. However, a point electrode cannot be used to compute the virtual current with the present finite volume method. Therefore, we simulated an area-electrode with a small finite size. Since the physical extents of the electrode were just about 5.0% and 1.05% of the circumferential and the axial dimensions ($L/R = 14.96$) of the computation domain, respectively (see Fig. 7), a large number of grid points were required to resolve the stiff potential field near the electrode. To alleviate this problem, a dense grid was located near the wall (or the electrode).

The current on the electrode could not have a step increment because of the finite nature of the numerical method. If a finite increment were to be imposed as the boundary condition, the grid size dependency of the solution would become dominating as the increment increased. To resolve this problem, the boundary current was smoothed. The ideal method of smoothing uses a unitary function, whose Fourier transform has a value only at the zero wave number (Lighthill, 1980). Unitary functions, however, consist of improper integrals and cannot be easily implemented. Therefore, a polynomial curve fit was used, which smoothed the profile of the current up to the first-order derivatives. It can be represented by

$$E(z)L_e = \begin{cases} 0 & \text{for } \bar{z} \leqslant -\frac{L_e}{2} - \beta, \\ -\frac{1}{4\beta^3}\left(\bar{z} + \frac{L_e}{2}\right)^3 + \frac{3}{4\beta}\left(\bar{z} + \frac{L_e}{2}\right) + \frac{1}{2} & \text{for } -\frac{L_e}{2} - \beta \leqslant \bar{z} \leqslant -\frac{L_e}{2} + \beta, \\ 1 & \text{for } -\frac{L_e}{2} + \beta \leqslant \bar{z} \leqslant \frac{L_e}{2} - \beta, \\ \frac{1}{4\beta^3}\left(\bar{z} - \frac{L_e}{2}\right)^3 - \frac{3}{4\beta}\left(\bar{z} - \frac{L_e}{2}\right) + \frac{1}{2} & \text{for } \frac{L_e}{2} - \beta \leqslant \bar{z} \leqslant \frac{L_e}{2} + \beta, \\ 0 & \text{for } \bar{z} \geqslant \frac{L_e}{2} + \beta, \end{cases} \tag{33}$$

where β is the diffusion parameter, which determines the fitting length, and $\bar{z} = z + \frac{L_z}{2}$. $E(\theta)$ can be constructed in a similar manner. The product of $E(\theta)$ and $E(z)$ was used as the boundary condition for $E(\theta, z)$ (see Eq. (30)). The effect of the diffusion parameter was tested for $\beta = 0.04$ (about 25% of the length of the electrode), $\beta = 0.08$, and $\beta = 0$. The potential value at the center of the electrode differed by less than 0.5%, regardless of the value of β. In the present study, $\beta = 0.04$.

The total numerical accuracy can be estimated from the error obtained by integrating the virtual current on the symmetric plane using the continuity of the virtual current (see Fig. 7):

$$\left| R\int_0^{L_z}\int_0^{\pi} E(\theta, z)\,\mathrm{d}\theta\,\mathrm{d}z - \left(\int\int \frac{\partial G}{\partial y}\bigg|_{\theta=0} \mathrm{d}z\,\mathrm{d}r + \int\int \frac{\partial G}{\partial y}\bigg|_{\theta=\pi} \mathrm{d}z\,\mathrm{d}r \right) \right|. \tag{34}$$

In this study, the errors appeared to be less than 10^{-8} for all of the computations.

3.2.2. Numerical results and discussions

The virtual potential and previous velocity fields, which were computed on the different grid systems, were interpolated into an orthogonal domain to calculate the weight functions and to

predict the flowmeter signals. The target orthogonal domain had the same axial length as the effective flowmeter window (see Fig. 7).

A tangent hyperbolic function (Thompson et al., 1985) was used to produce the grid in the radial direction of the orthogonal domain. This function was modified to give a dense grid near the wall (or the electrode),

$$\frac{r(\xi)}{R} = \frac{1}{\alpha_r} \tanh\left(\frac{\xi}{2} \ln\frac{1+\alpha_r}{1-\alpha_r}\right), \tag{35}$$

where α_r is the stretching parameter in the radial direction. As α_r goes to 1, the grid becomes more clustered towards the wall. In the axial and azimuthal directions, a different stretching function was used,

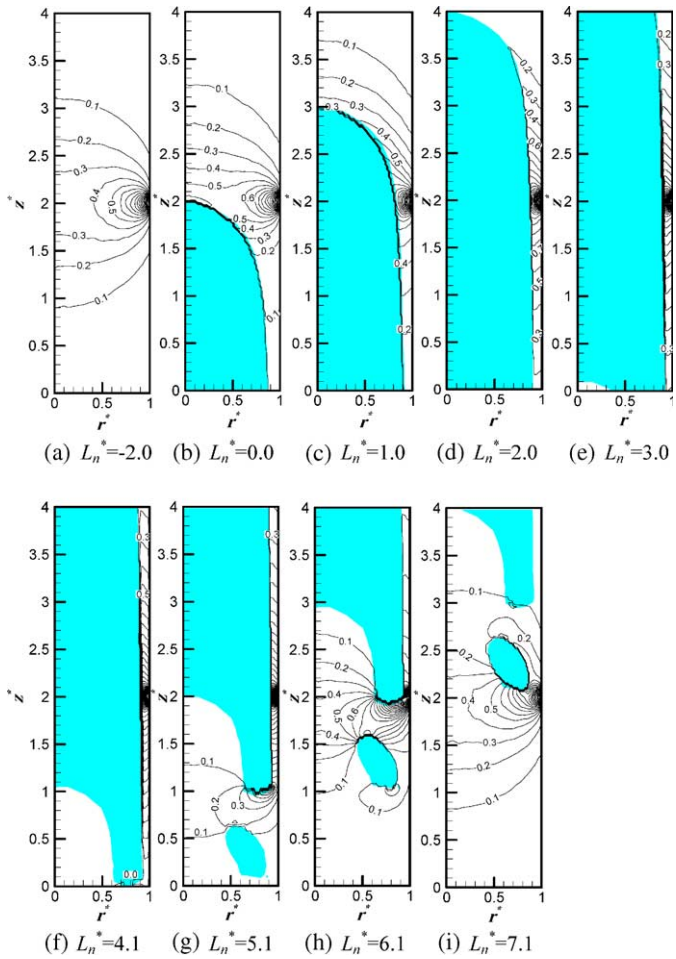

Fig. 8. Contour plots of the normalized axial weight function $W_z(r,z)/B$ (long bubble): contours are advanced by 0.1.

$$\frac{z(\varsigma)}{L_z} = \frac{1}{2}\left(1 - \ln\frac{1+\alpha_z(1-2\varsigma)}{1-\alpha_z(1-2\varsigma)} \Big/ \ln\frac{1+\alpha_z}{1-\alpha_z}\right), \tag{36}$$

$$\theta(\eta) = \frac{\pi}{2}\left(1 - \ln\frac{1+\alpha_\theta(1-2\eta)}{1-\alpha_\theta(1-2\eta)} \Big/ \ln\frac{1+\alpha_\theta}{1-\alpha_\theta}\right), \tag{37}$$

where α_z and α_θ are the stretching parameters in the axial and azimuthal directions, respectively. As α_z and α_θ go to 1, the grid becomes denser around the electrode placed at the center of the orthogonal domain. The orthogonal domain was created with $50\times100\times100$ grid points in the radial, azimuthal, and axial directions, respectively, $\alpha_r = 0.95$, $\alpha_\theta = 0.9$ and $\alpha_z = 0.9$, which were the same parameters used by Ahn et al. (2003a). The inverse distance method was used for the interpolation,

$$\varphi_d = \frac{\sum w_s \varphi_s}{\sum w_s}, \tag{38}$$

where φ_d and φ_s are the values of the variables at the destination point and the source point, respectively, w_s is the weighting function defined as

$$w_s = d^{-3.5} \tag{39}$$

and d is the distance between the source point and the destination point.

Figs. 8 and 9 show the axial weight functions (see Eq. (10)) divided by the magnetic flux density B for the long and short bubble cases, respectively. The axial weight functions varied with the bubble position relative to the electrode position, which was represented by its nose position $L_n^* = L_n/R$. The axial weight function was the azimuthal average of the y-component of the virtual current density. A value 0.5 of the axial weight function was corresponding to 1.24% of the virtual current density imposed at the electrode. For practical applications, sensitivity variations are to be expected from the non-uniformity of the magnetic field. However, non-uniformities in regions where the axial weight function is less than 0.5 do not affect the sensitivity (Bevir, 1970).

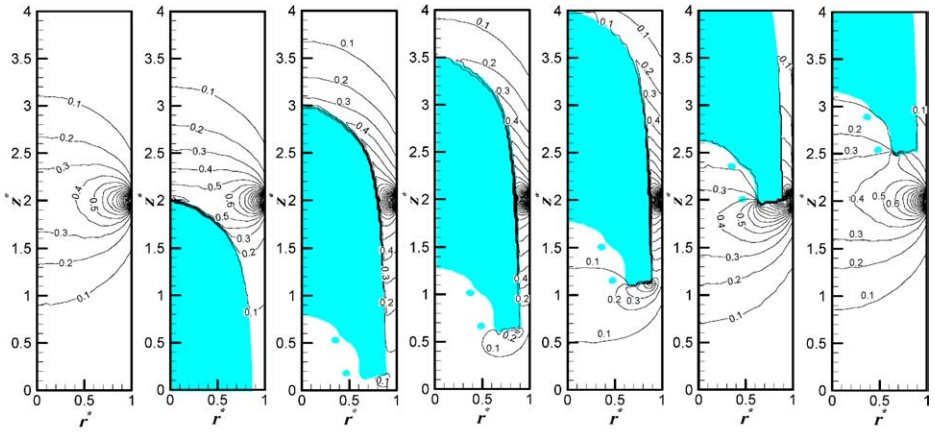

Fig. 9. Contour plots of the normalized axial weight function $W_z(r,z)/B$ (short bubble): contours are advanced by 0.1.

For single-phase flows (plot a in Figs. 8 or 9), the axial weight function was symmetric with respect to $z^* = z/R = 2$ (the electrode plane). Plots (b) to (i) in Fig. 8 and (b) to (g) in Fig. 9, which correspond to a rising slug bubble, show an asymmetric distribution of the axial weight function. When the axial weight function distributions for slug flows were compared to those obtained for single-phase flows, the effective region over which the weight function had a significant value changed with the bubble position. This was because the virtual current detoured towards the path with the least resistance. As the region further behind the Taylor bubble tail moved closer to the electrode, the axial weight function distributions approached the values obtained for the single-phase case.

Figs. 10 and 11 show the radial weight functions (see Eq. (9)) divided by the magnetic flux density B. The radial weight functions also varied with the nose position $L_{\mathrm{n}}^* = L_{\mathrm{n}}/R$. Half of the radial weight function, or the azimuthal average of the z-component of the virtual current density, was also 1.24% of the virtual current density imposed at the electrodes.

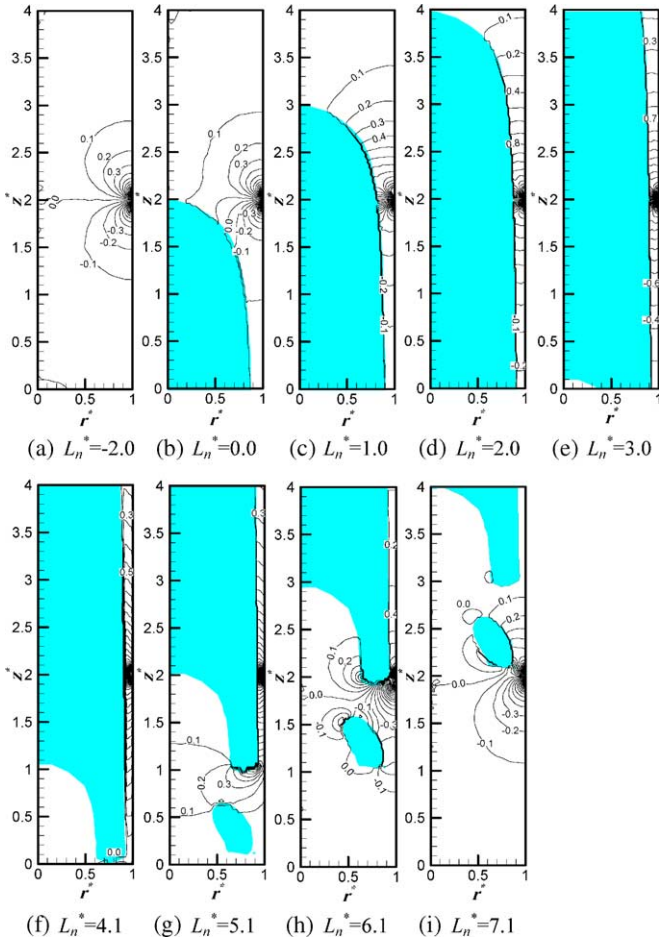

Fig. 10. Contour plots of the normalized radial weight function $W_r(r,z)/B$ (long bubble): contours are advanced by 0.1.

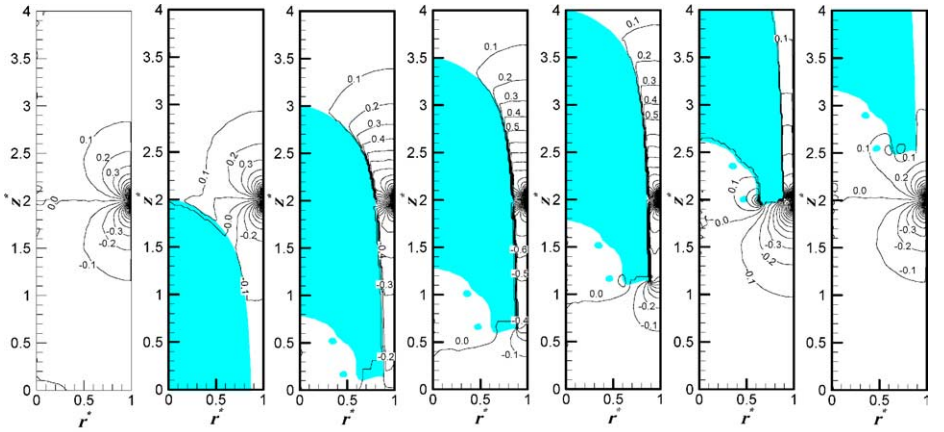

Fig. 11. Contour plots of the normalized radial weight function $W_r(r,z)/B$ (short bubble): contours are advanced by 0.1.

For single-phase flows (plot a in Figs. 10 or 11), the distribution of the radial weight function related to the z -component of the virtual current was anti-symmetric with respect to $z^* = z/R = 2$ (the electrode plane). These plots show horizontal stagnant lines (zero lines) over which the radial velocities do not contribute to the output signal. The radial weight function was more localized around the electrode than the axial weight function, so the radial velocity in the region around the pipe centerline did not have much effect. As the region further behind the Taylor bubble tail moved closer to the electrode, distributions of the radial weight function also approached the values obtained for the single-phase case, similar to the axial weight function.

The axial weight density function $p(z^*)$ in Eq. (16), the radially weighted axial velocity $\bar{v}_z(z^*)$ in Eq. (18), and the liquid mean velocity $v_{\mathrm{mTP}}(z^*)$ for rising slug bubbles are shown in Figs. 12 and 13 for the long and short bubble cases, respectively. The axial weight density functions were compared to those obtained for single-phase flow ($L_{\mathrm{n}}^* = -2.0$). The detouring of the virtual current caused the axial weight density function to increase in the liquid slug and to decrease in the liquid film as compared to the single-phase flow values. A change in the slope of $p(z^*)$ was evident at the nose and tail of the Taylor bubble or the electrode. For the short bubble, there was a case where the slope changed at three points (plot (b)) due to its short length, which indicated that both the nose and tail of the Taylor bubble were within the effective flowmeter window. The slope change was also due to the detouring of the virtual current.

The velocities used in Eqs. (15), (18) and (19) were obtained using the interpolation method stated previously (Eqs. (38) and (39)). The velocity field obtained from the numerical simulation (see Section 3.1) was interpolated onto an $r-z$ structured plane (50×100 grid points for N_r and N_z) of the aforementioned three-dimensional target domain. Figs. 12 and 13 show that the radially weighted axial velocity $\bar{v}_z(z^*)$ was slightly smaller (larger in absolute value) than the liquid mean velocity $v_{\mathrm{mTP}}(z^*)$ in the liquid film, except around electrode ($z^* = 2$) (see Figs. 12(b) and 13(b)). This was due to the fact that the radial profile of the axial weight function far from the electrode plane had a maximum value at the interface, but the position of the maximum value moved closer

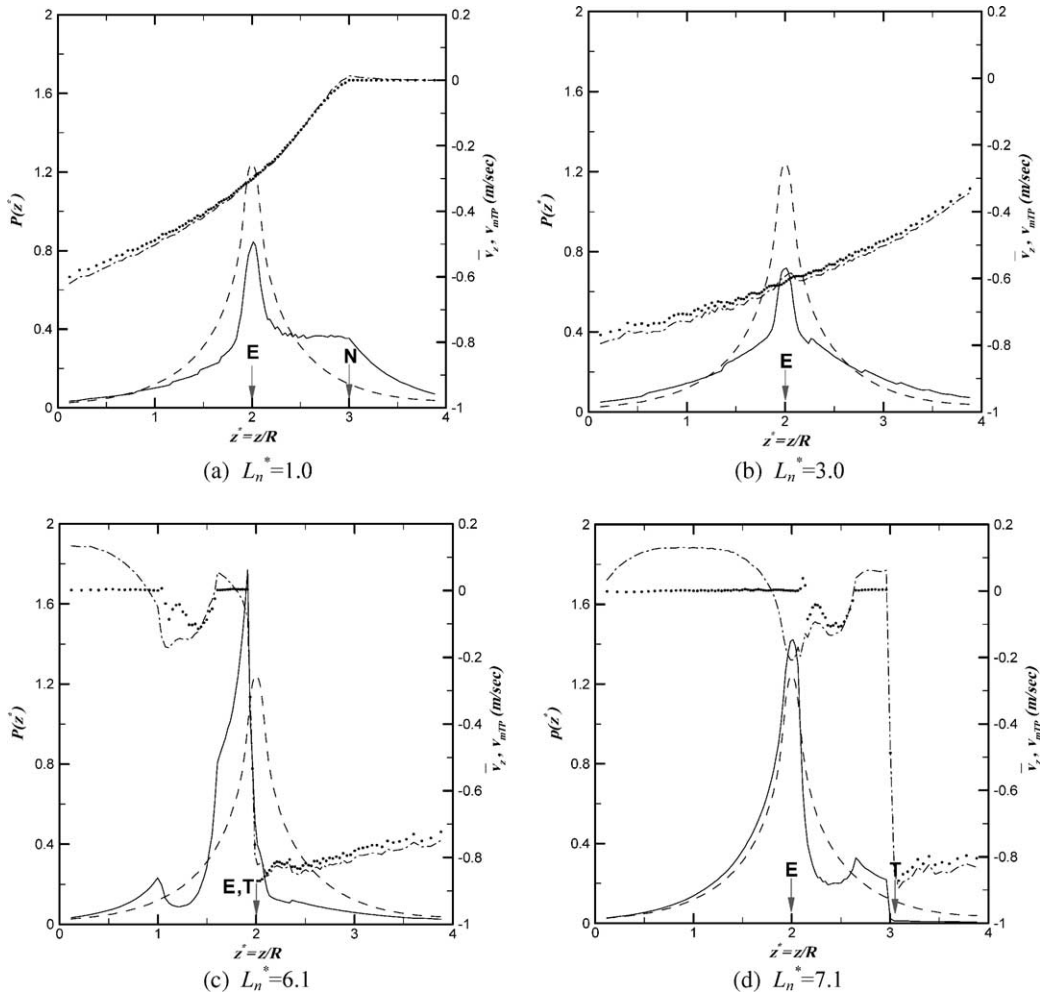

Fig. 12. Axial weight density function and liquid mean velocity profiles (long bubble): —, $P(z^*)$ for slug flow cases; – – – $P(z^*)$ for single-phase flow case ($L_{\mathrm{n}}^* = -2.0$); -·-·-·, $\bar{v}_z(z^*)$; · · ·, $v_{\mathrm{mTP}}(z^*)$, (E: electrode, T: tail, N: nose).

to the wall as it approached the plane. The difference between $\bar{v}_z(z^*)$ and $v_{\mathrm{mTP}}(z^*)$ was within 2.5% in the film (the rms value of the difference with respect to the maximum v_{mTP}). However, $\bar{v}_z(z^*)$ was larger than $v_{\mathrm{mTP}}(z^*)$ in the wake zone, because the upward velocities around pipe axis were highly weighted (see Figs. 5, 8 and 9).

A measure of the amount of detouring by the virtual current can be obtained from the proportion of the axial weight density function for the liquid slug, $\eta_p(L_{\mathrm{n}}^*)$, defined by

$$\eta_p = \frac{\int_{\Omega_S} p(z^*)\,\mathrm{d}z^*}{\int_{-\infty}^{\infty} p(z^*)\,\mathrm{d}z^*} = \int_{\Omega_S} p(z^*)\,\mathrm{d}z^*, \tag{40}$$

where Ω_S is the liquid single-phase region. The relative proportion $\eta_p(L_{\mathrm{n}}^*)$ of the axial weight density function for the liquid slug is shown in Fig. 14. Electromagnetic flowmeters have an

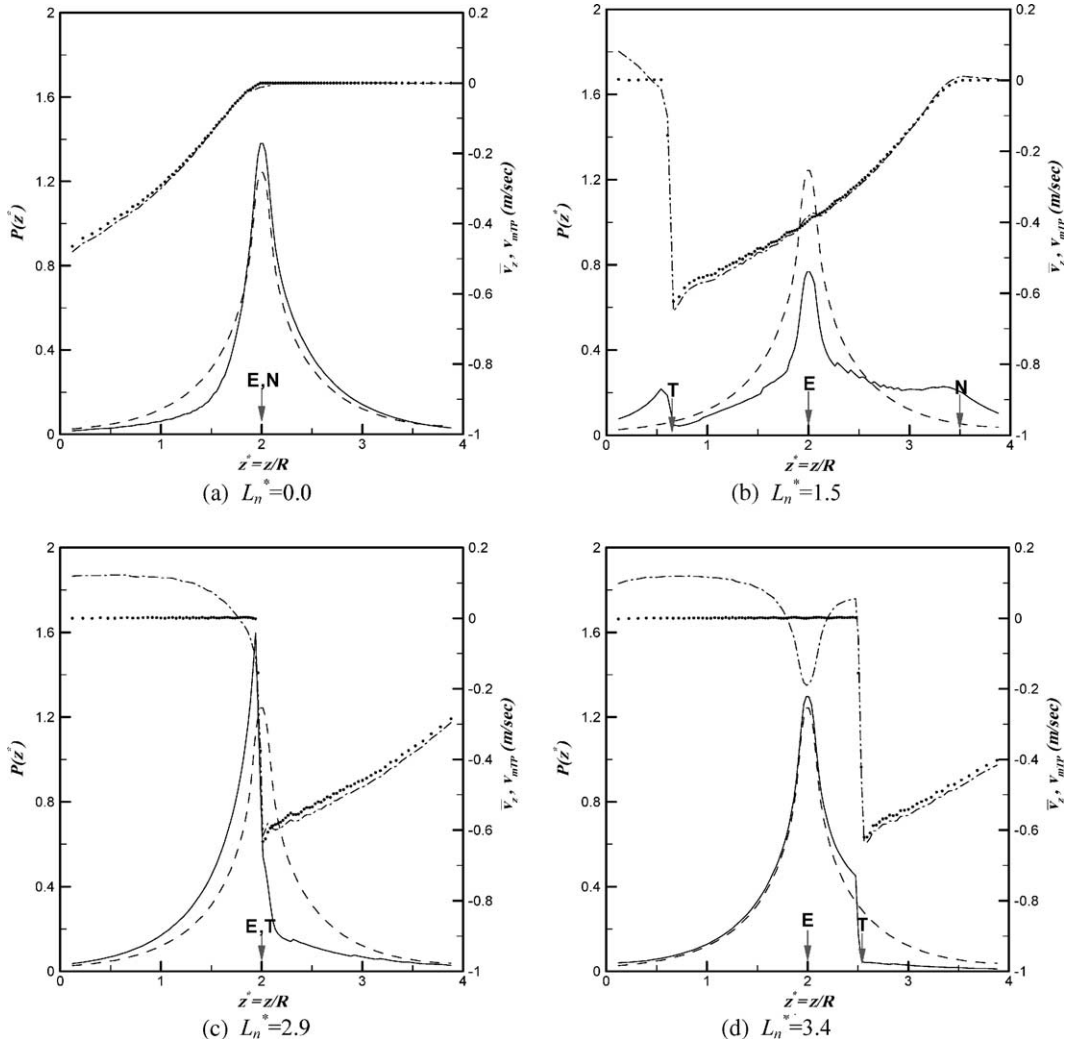

Fig. 13. Axial weight density function and liquid mean velocity profiles (short bubble): —, $P(z^*)$ for slug flow cases; – – – $P(z^*)$ for single-phase flow case ($L_{\mathrm{n}}^* = -2.0$); ·-·-·-, $\bar{v}_z(z^*)$; · · ·, $v_{\mathrm{mTP}}(z^*)$, (E: electrode, T: tail, N: nose).

effective window size around the electrode. Therefore, the decreasing curves of $\eta_p(L_{\mathrm{n}}^*)$ were always the same, because the flowmeter experienced the same situation each time and did not notice the effect of the bubble length when identical-shaped noses were approaching the electrode. However, for bubbles that were shorter than the effective window size, there was a departing point (at $L_{\mathrm{n}}^* \approx 1$ for the present short bubble) from the curve according to their length. The increasing pattern of the $\eta_p(L_{\mathrm{n}}^*)$ curves was very similar, although there was a slight dependence on the void fraction at the slug bubble tail and on the daughter bubbles. A similar procedure can be applied to the radial weight function to obtain $q(z^*)$ in Eq. (17), $\bar{v}_r(z^*)$ in Eq. (19), and the relative proportion of $q(z^*)$ for the liquid slug (not shown here).

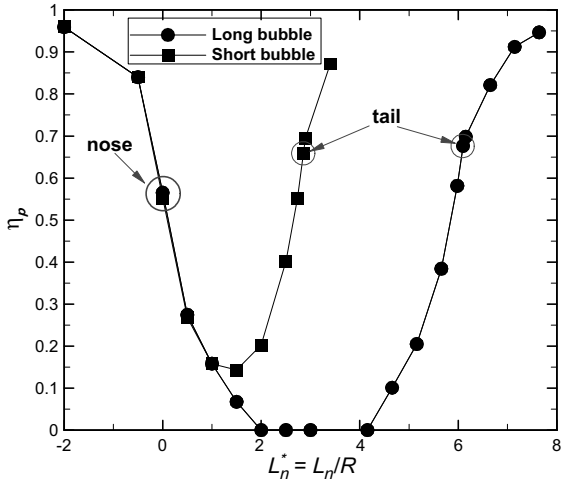

Fig. 14. Plot of the single-phase contribution on $P(z^*)$, $\eta_p(L_n^*)$ with respect to the bubble location L_n^*.

A proper localization parameter χ is required to avoid introducing errors in the time-averaged liquid flow rate. Ahn et al. (2003b) modeled the localization parameter by approximating the Taylor bubble as a stationary finite-cylinder and assuming that the liquid velocity field around the bubble tail behaved as follows:

$$\mathbf{v} = \begin{cases} (0,0,u) & \text{if } z^* > L_t^*, \\ (0,0,(1-\varepsilon)u) & \text{if } z^* < L_t^*, \end{cases} \tag{41}$$

where u is the uniform film velocity, ε is the void fraction, and $L_t^* = L_t/R (0 < L_t^* < L_z^*)$ is the tail location, as shown in Fig. 7. Ahn et al. (2003b) focused on the signal behavior around the tail of Taylor bubbles that were larger than the effective window size. Using Eq. (15), their suggested localization parameter was

$$\chi = \begin{cases} \frac{1}{1-\varepsilon\eta_P} & \text{if } L_t^* \leqslant L_z^*/2 \\ \frac{1-\varepsilon}{1-\varepsilon\eta_P} & \text{if } L_t^* > L_z^*/2. \end{cases} \tag{42}$$

Fig. 15(a) and (b) depict the localization parameters calculated from Eq. (15) with or without the radial velocity $\bar{v}_r(z^*)$, and by Eq. (42) with ε at the tail, at various bubble locations for both long and short bubbles, respectively. As the Taylor bubbles rose, the localization parameter for both cases remained almost constant when $L_n^* \leqslant L_b^* - L_z^*/2$, and increased to its peak value when the exact trailing edge reached the electrode ($L_n^* = 6.1$ and 2.9 for the long and short bubbles, respectively). Then the localization parameter abruptly fell in the liquid slug region. For single-phase and annular flows with constant δ^* the localization parameter is unity (Ahn et al., 2003a). However, for a slug flow with a continuously varying film thickness and accelerated developing flow characteristics in the effective window, the localization parameter was above unity in the film, i.e., by assuming $\chi = 1$ in the decomposition method used by Mi (1998), a significant error in the velocity estimate was inevitable, particularly around the tail. When compared to the χ model used by Ahn et al. (2003b), the present results gave larger χ values. This is why the present results are

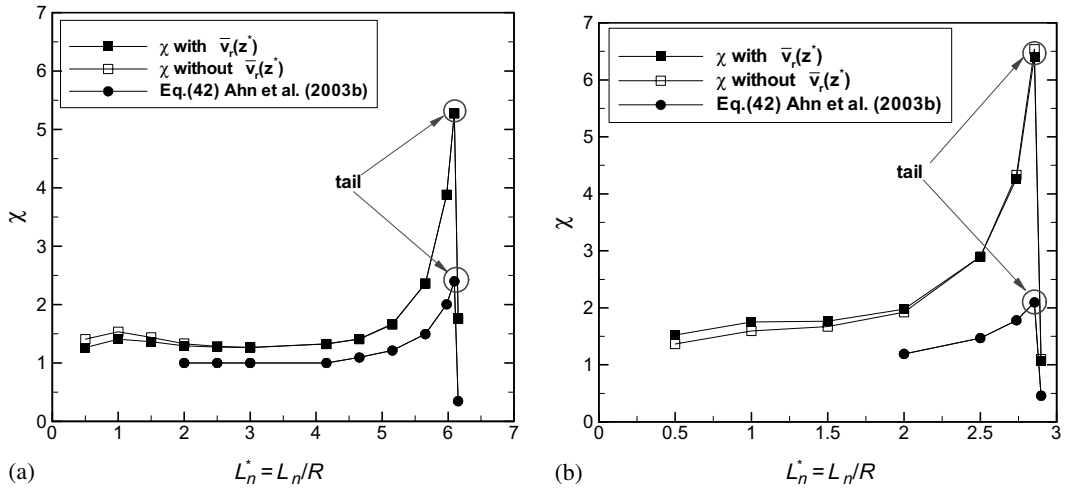

Fig. 15. Plot of the localization parameter with respect to the bubble location, L_n^*: (a) long bubble, (b) short bubble.

more realistic: they consider the actual shape of the rising Taylor bubble, the increasing axial speed in the liquid film, and the radial variation of the axial velocity in the wake zone. (The large difference between $v_{mTP}(z^*)$ and $\bar{v}_z(z^*)$ in the wake zone contributes to the difference between the χ model and the present results.) For instance, the modeled χ was unity when $L_z^*/2 \leqslant L_n^* \leqslant L_b^* - L_z^*/2$ and the bubble was longer than the window size (i.e., when the cylinder bubble occupied the entire effective window, which is the same situation that is encountered in annular flow). The present results gave χ almost equal to 1.3 because they considered the film thinning and, therefore, the increasing axial speed in the liquid film. On the other hand, the peak value of χ was smaller for a long bubble than for a short bubble. This was mainly due to the faster rate of increase in the speed of the liquid film in the effective window for the short bubble, as shown in Figs. 12(c) and 13(c). Fig. 15 indicates that the radial velocity had little influence on the localization parameter, except for lower values of L_n^* (Lower values L_n^* indicate that the electrode was positioned near the bubble nose, where there are relatively large radial velocities). If there is sufficient liquid superficial velocity, the effect of the radial velocity around the nose will also be negligible.

The flow pattern coefficient f must be known in advance to calibrate a current-sensing flowmeter. The coefficients shown in Figs. 16 and 17 can be obtained from the virtual potential differences between the two electrodes. The coefficient f can be viewed as a function of the non-dimensionalized film thickness δ^* at the electrode as well as the non-dimensionalized bubble nose position L_n^* for a rising slug bubble. Fig. 16 shows the flow pattern coefficient as a function of the bubble location, L_n^*. The coefficient f was almost unity when $L_n^* < 0$ or $L_n^* > L_b^* + 0.5$, which indicated that the current-sensing flowmeter recognized this flow pattern as single-phase flow. The increasing shape of each curve is always the same, for the same reason as given for the $\eta_p(L_n^*)$ curves. Bubbles that were shorter than the effective window size had a departing point ($L_n^* \approx 1$ for the present short bubble) from the curve according to their length. The decreasing pattern of the curves was also very similar, although there was a slight dependence on the void fraction at the slug bubble tail and on the daughter bubbles. The peak values were $f = 2.22$ at $L_n^* = 4.66$ for

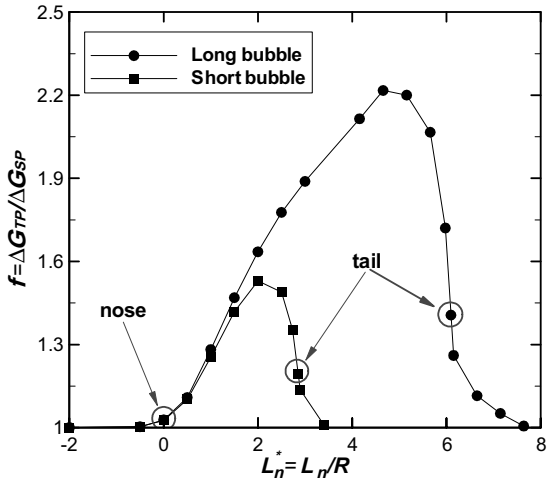

Fig. 16. Flow pattern coefficient f as a function of the bubble location L_n^*.

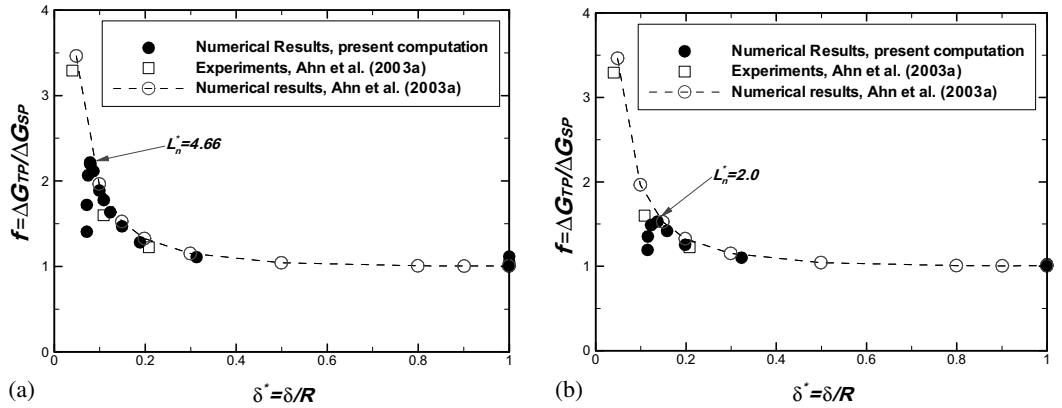

Fig. 17. Flow pattern coefficient f as a function of the non-dimensionalized film thickness δ^*: (a) long bubble, (b) short bubble.

the long bubble, and $f = 1.53$ at $L_n^* = 2.0$ for the short bubble. For bubbles longer than the window size, the maximum value occurred when the bubble tail reached the lowest plane of the effective window and the bubble occupied the entire window. For shorter bubbles, the maximum value occurred after at least 50% of the bubble had passed the electrode (69% for the present short bubble). Fig. 17(a) and (b) show the present predictions for both slug bubbles, along with the experimental and numerical results for annular flows by Ahn et al. (2003a). These figures illustrate the errors that are introduced when one simply uses the f value of the corresponding annular flow instead of that of the slug flow. The peak values are at $\delta^* = 0.079$ for the long bubble and $\delta^* = 0.115$ for the short bubble. When $\delta^* > 0.3$, the flow pattern coefficients for the long and short bubble cases are nearly 1.0, since the virtual potential decreases sharply with the distance from the

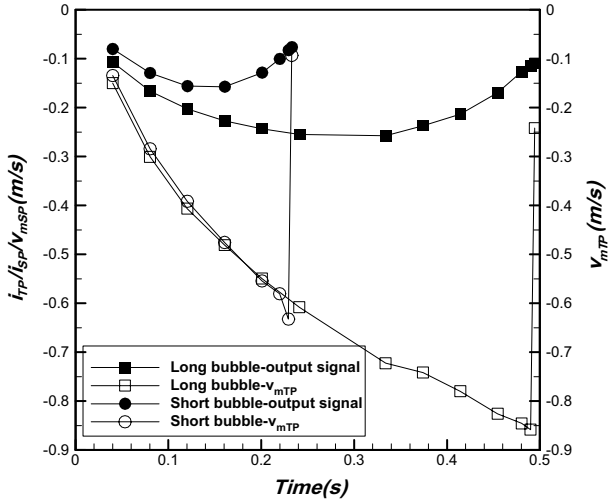

Fig. 18. Normalized output signal, $\frac{i_{TP}\cdot v_{mSP}}{i_{SP}}\left(=\frac{v_{mTP}}{f\cdot\chi}\right)$ compared with liquid mean velocity on the electrode plane for a current-sensing flowmeter.

electrode and the electrode potential cannot be disturbed by obstacles positioned near the pipe center. Assuming that the slug flow behaves as an annular flow when $\delta^* > 0.3$, the error in the flow coefficient f is within 3% for both slug flow cases. When δ^* is greater than 0.079 for the long bubble and greater than 0.115 for the short bubble, which correspond to the locations of the peaks, the errors are within 7.4% and 4.8%, respectively. As δ^* decreases from the critical values where the flow pattern coefficients reach their maximum values, the coefficients abruptly decrease. This is due to the large virtual current that flows towards the liquid slug in the lower window, even

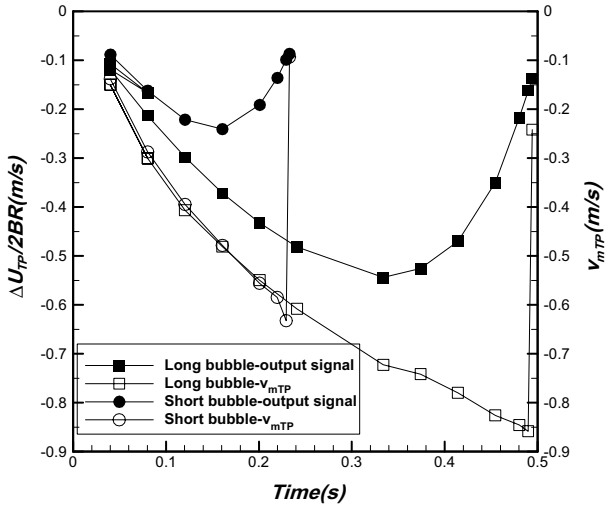

Fig. 19. Normalized output signal, $\frac{\Delta U_{TP}}{2BR}\left(=\frac{v_{mTP}}{\chi}\right)$ compared with liquid mean velocity on the electrode plane for a voltage-sensing flowmeter.

though the electrode sees the thin liquid film. The deviation between the slug and annular flows increases rapidly.

Figs. 18 and 19 give time series of the non-calibrated outputs and the liquid mean velocities on the electrode plane, v_{mTP}, for the current-sensing (Eq. (14)) and voltage-sensing (Eqs. (1) and (8)) flowmeters. For both types of flowmeters, a significant error will be included in the results if the effect of the calibration parameter(s) is neglected. Therefore, it is very important to obtain the localization parameter and the flow pattern coefficient, and to calibrate the flowmeter for each flow pattern. To do so, information about the bubble position must be supplied using, for example, an impedance meter. The slug flow experiment including the measurement of bubble position will be carried out with the current-sensing flowmeter and two impedance meters. The experimental result will be compared with this result and reported in the near future.

4. Conclusions

The theory of current-sensing flowmeters with high temporal resolution was applied to two-phase slug flow with fast transients. The velocity fields and Taylor bubble shapes were computed using the volume-of-fluid (VOF) model for long and short bubbles ($Eo = 87$ and $Mo = 1.4 \times 10^{-11}$) to simulate the response of conventional voltage-sensing and current-sensing flowmeters in a slug flow. These results were compared to existing experimental and analytical data and had a good agreement. The three-dimensional virtual potential distributions for small finite electrodes were also computed with a finite volume method using the computed bubble shape. The axial weight, axial weight density, and radial weight functions were defined and computed from the gradient of the virtual potential, which corresponded to the velocity contribution to the flowmeter output at each position. A time series of the flowmeter output was predicted for both types of flowmeter.

A calibration procedure for both types of flowmeter was described. A localization parameter χ was introduced to remove the error caused by rapidly accelerating and decelerating flows, such as with a slug flow. The localization parameter was provided for both types of flowmeter as a function of the normalized bubble nose position, L_n^*, relative to the electrode position. The localization parameter was almost constant ($\approx$1.3) when $L_n^* \leqslant L_b^* - L_z^*/2$, provided that the bubble was longer than the effective window size ($L_z^* = 4$) of the flowmeter. The peak value of χ occurred at the bubble tail because of detouring by the virtual current and the abrupt change in the axial liquid velocity. The radial velocity had little effect on χ. The flow pattern coefficient f was calculated and provided to simplify the calibration process for current-sensing flowmeters. The value of f for the slug flow was almost unity when $\delta^* > 0.3$ or $L_n^* < 0$ or $L_n^* > L_b^* + 0.5$. Before the wake region started to occupy the effective window or the flow pattern coefficient f reached its maximum value, the slug flow could be treated as an annular flow to determine f with only a 7.4% or 4.8% error for the long and short bubbles, respectively.

The non-calibrated velocities or normalized outputs were compared to the actual liquid velocities for both types of flowmeter to demonstrate the significance of the errors that were introduced by neglecting the localization parameter and/or the flow pattern coefficient. Once a flowmeter signal is obtained experimentally, these calibration parameters will prove useful when calculating an accurate liquid mean velocity for slug flow.

Acknowledgements

This work was supported by the National Research Laboratory of the Korean Ministry of Science and Technology, and by Brain Korea 21 administered by the Korean Ministry of Education.

References

Ahn, Y.C., Oh, B.D., Kim, M.H., 2003a. A current-sensing electromagnetic flowmeter for two-phase flow and numerical simulation of the three-dimensional virtual potential distribution. Part I. Fundamentals and annular flow. Meas. Sci. Technol. 14, 239–250.

Ahn, Y.C., Oh, B.D., Kim, M.H, 2003b. An advanced electromagnetic flowmetry for two-phase flow (KL-13; Keynote lecture). In: Proceedings of the 10th International Topical Meeting on Nuclear Reactor Thermal Hydraulics, Seoul, Korea, October 5–11.

Anglart, H., 2001. Mechanistic modeling of slug flows. Ph.D. Dissertation, Rensselaer Polytechnic Institute, USA.

Bevir, M.K., 1970. The theory of induced voltage electromagnetic flowmeters. J. Fluid Mech. 43, 577–590.

Bugg, J.D., Mack, K., Rezkallah, K.S., 1998. A numerical model of Taylor bubbles rising through stagnant liquids in vertical tubes. Int. J. Multiphase Flow 24, 271–281.

Cha, J.E., Ahn, Y.C., Kim, M.H., 2002. Flow measurement with an electromagnetic flowmeter in two-phase bubbly and slug flow regimes. Flow Meas. Instrum. 12, 329–339.

DeJesus, J.M., 1997. An experimental and numerical investigation of two-phase slug flow in a vertical tube. Ph.D. Dissertation, University of Toronto, Canada.

DeJesus, J.M., Ahmad, W., Kawaji, M., 1995. Experimental study of flow structure in vertical slug flow. In: Advances in Multiphase Flow. Elsevier, Amsterdam, pp. 105–118.

Dumitrescu, D.T., 1943. Strmung an einer Luftblase im senkrechten Rohr. Z. Angew. Math. Mech. 23, 139–149.

Glasstone, S., 1942. An Introduction to Electrochemistry. Van Nostrand, New York.

Hirt, C.W., Nichols, B.D., 1981. Volume of fluid (VOF) method for the dynamics of free boundaries. J. Comput. Phys. 39, 201–225.

Kawaji, M., DeJesus, J.M., Tudose, G., 1996. Investigation of flow structures in vertical slug flow. In: Proceedings of the Japan US Seminar on Two-Phase Flow Dynamics, Fukota, Japan.

Knoll, K.E., 1991. Investigation of an electromagnetic flowmeter for gas liquid two-phase flow measurement. Trans. ANS 64, 720–721.

Kothe, D.B., Rider, W.J., Mosso, S.J., Brock, J.S., 1996. Volume tracking of interfaces having surface tension in two and three dimensions. Technical Report AIAA 96-0859, AIAA (1996). [Presented at the 34rd Aerospace Sciences Meeting and Exhibit].

Lighthill, M.J., 1980. Introduction to Fourier Analysis and Generalised Functions. Cambridge University Press, London.

Lim, K.W., Chung, M.K., 1998. Relative errors in evaluating the electromagnetic flowmeter signal using the weight function method and the finite volume method. Flow Meas. Instrum. 9, 229–235.

Lonsdale, 1993. An algebraic multigrid solver for Navier–Stokes equations on unstructured meshes. Int. J. Numer. Meth. Heat Fluid Flow 3, 3–14.

Macdonald, J.S., 1987. Impedance Spectroscopy: Emphasizing Solid Materials and Systems. John Wiley & Sons, New York.

Mao, Z.S., Dukler, A.E., 1991. The motion of Taylor bubbles in vertical tubes. II. Experimental data and simulations for laminar and turbulent flow. Chem. Eng. Sci. 46, 2055–2064.

Mi, Y., 1998. Two-phase flow characterization based on advanced instrumentation, neural networks, and mathematical modeling. Ph.D. Dissertation, Purdue University, USA.

Mi, Y., Ishii, M., Tsoukalas, L.H., 2001. Investigation of vertical slug flow with advanced two-phase flow instrumentation. Nucl. Eng. Des. 204, 69–85.

O'Sullivan, V.T., Wyatt, D.G., 1983. Computation of electromagnetic flowmeter characteristics from magnetic field data. III. Rectilinear weight functions. J. Phys. D: Appl. Phys. 16, 1461–1476.

Patanker, S.V., 1980. Numerical Heat Transfer and Fluid Flow. McGraw-Hill, NewYork.

Polonsky, S., Shemer, L., Barnea, D., 1999. An experimental study of the relation between the Taylor bubble motion and the velocity field ahead of it. Int. J. Multiphase Flow 25, 957–975.

Saad, Y., 1996. Iterative Methods for Sparse Linear Systems. PWS, Boston.

Shercliff, J.A., 1954. Relation between the velocity profile and the sensitivity of electromagnetic flowmeters. J. Appl. Phys. 25, 817–818.

Shercliff, J.A., 1962. The Theory of Electromagnetic Flow Measurement. Cambridge University Press.

Thompson, J.F. et al., 1985. Numerical Grid Generation: Foundations and Applications. North-Holland, New York.

Tsiknakis, E., 1988. Novel excitation waveforms and signal processing for electromagnetic flowmetering. Ph.D. Dissertation, University of Bradford, UK.

van Doormaal, J.P., Raithby, G.D., 1984. Enhancements of the SIMPLE method for predicting incompressible fluid flows. Numer. Heat Transfer 7, 147–163.

White, E.T., Beardmore, R.H., 1962. The velocity of rise of single cylindrical air bubbles through liquids contained in vertical tubes. Chem. Eng. Sci. 17, 351–361.

Wyatt, D.G., 1986. Electromagnetic flowmeter sensitivity with two-phase flow. Int. J. Multiphase Flow 12, 1009–1017.

Yang, H.Q., Przekwas, A.J., 1998. Computational modeling of microfluid devices with free surface devices with free surface liquid handling. CFDRC, PA-98-11.

Yu, P.L., Zhang, C.Y., Zmood, R.B., 1997. Wide-band low-input-impedance trans-impedance amplifiers for instrumentation application. Meas. Sci. Technol. 8, 1351–1355.

Zhang, X.Z., 1997. The effect of the phase distribution on the weight function of an electromagnetic flow meter in 2D and in the annular domain. Meas. Sci. Technol. 8, 1285–1288.

Zhang, X.Z., 1998. 2D analysis for the virtual current distribution in an electromagnetic flow meter with a bubble at various axis positions. Meas. Sci. Technol. 9, 1501–1505.